Science
AAAS

Visualizing the Electron Scattering Force in Nanostructures

Chenggang Tao, *et al.*

Science **328**, 736 (2010);
DOI: 10.1126/science.1186648

Visualizing the Electron Scattering Force in Nanostructures

Chenggang Tao,* W. G. Cullen, E. D. Williams†

In nanoscale metal wires, electrical current can cause structural changes through electromigration, in which the momentum of electrons biases atomic motion, but the microscopic details are complex. Using in situ scanning tunneling microscopy, we examined the effects of thermally excited defects on the current-biased displacement of monatomic islands of radius 2 to 50 nanometers on single-crystal Ag(111). The islands move opposite to the current direction, with velocity varying inversely with radius. The force is thus in the same direction as electron flow and acts on atomic defect sites at the island edge. The unexpectedly large force on the boundary atoms can be decreased by over a factor of 10 by adding a mildly electron-withdrawing adsorbate, C_{60}, which also modifies the step geometry. The low coordination of the identified scattering sites is the likely origin of the large force.

When electrical current passes through a wire, the current carriers can scatter off of interfaces or defects and transfer momentum to atoms in these regions, resulting in biased diffusion of mobile atoms. This electromigration force is so small that it may result in a directional bias in fewer than one in 10 million diffusion steps, but the cumulative effects generate micrometer-scale voids in the small metal wires in modern electronics (*1*, *2*). At the nanoscale, electromigration forces may be equally destructive but also provide opportunities for control of structure as in nanogap formation (*3*), for driving dopants into nanowires (*4*), and for coupling electrical signals to atomic fluctuations (*5*, *6*). We used scanning tunneling microscopy (STM) to observe the biased displacement of metallic islands in the presence of an applied current (Fig. 1A) so as to correlate the magnitude of the electromigration force to specific atomic structures, in this case "kink" sites at step edges. Using a step-continuum analysis, we quantified the site-resolved atomic force and found that the electromigration effects are much stronger than had been expected theoretically for non-kinked step edges.

Observations of mass diffusion due to electromigration under extremely high current densities ($>10^{13}$ A/m^2) have been presented for nano-gap formation (*7*, *8*); however, the complex geometries involved are not amenable to extracting quantitative information by modeling mass flow. The alternative approach of using theoretical understanding to quantify electron scattering at surface and interface defect sites requires an evolution from classical descriptions of bulk electromigration. The classical approaches use mean-field methods and must be reframed in terms of atomic structures, their local electron density, and nonequilibrium transport characteristics in order to understand electron scattering and electromigration in nanoscale structures.

In this study, the direct observation of the biased displacement of nanoscale structures produced a quantitative value for the electromigration force that can be identified with a specific type of structural defect, independent of assumptions about the bulk electrical properties. The test systems consist of silver (Ag) islands containing between 100 and 100,000 atoms. Electrical current (defined, as is standard, as being in the opposite direction to electron flow) through the substrate provides momentum transfer to the atoms in the islands, yielding a response that depends on the diffusion mechanism (*9*). Because surface diffusion is easiest for free atoms on terraces (D_T) or via thermally excited atomic-scale kinks at island edges (D_L), island displacement is most likely to occur via atomic attachment to or motion along the island edges. As a result, island motion does involve a shifting center of mass (COM) but not the net simultaneous displacement of all the atoms in the island.

The electromigration force can move an island via atomic motion in two different ways (Fig. 1B). Freely diffusing atoms on the terrace experience a drift velocity ($v_{EM} = D_T F/k_B T$, where F is the electromigration force, k_B is the Boltzmann constant, and T is temperature), creating a net flux of atoms onto one side of the island and a corresponding flux away from the opposite side. The resulting net displacement of the island's COM will be opposite the electromigration force, and (for a given electromigration force) the velocity of the island will be determined by the atomic flux per unit length of the island edge and

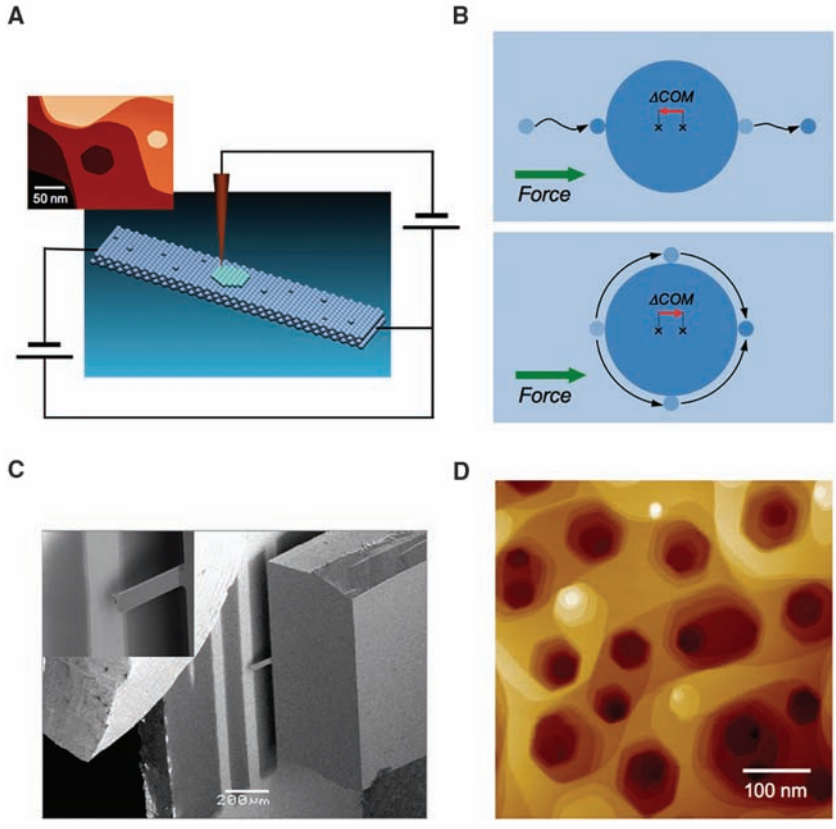

Fig. 1. (**A**) Schematic drawing of the experimental setup. (**B**) Schematic illustration of two mechanisms (top, attachment/detachment; bottom, edge diffusion); whichever mechanism biases the displacement of mass from one end of an island to the other shifts the COM. The starting positions of atoms are light blue; the end positions are dark blue. (**C**) SEM image of the experimental setup: Ag stripes and scanning tip. In the middle of the image, bright stripes are Ag stripes. STM images are obtained over the central part of the middle stripe as shown in the inset, which is a zoom-in SEM image of the STM tip and Ag stripe. (**D**) STM topography image of the surface Ag stripes after sputtering procedure. The image size is (500 × 500) nm^2, and the tunneling current is 52 pA with a sample bias of −1.87 V.

Materials Research Science and Engineering Center and Department of Physics, University of Maryland, College Park, MD 20742–4111, USA.
*Present address: Department of Physics, University of California at Berkeley, Berkeley, CA 94720, USA.
†Present address: BP, 1 St. James Square, London SW1Y 4PD, UK.

is thus independent of island size. Alternatively, the island will move if the force preferentially moves atoms along its edges from the "upwind" side to the "downwind" side. In this case, the displacement of the COM is opposite to that of terrace diffusion case. For edge diffusion, the island displacement is parallel to the electromigration force, and (for a given electromigration force) the COM velocity is determined by the island radius. A combination of the direction of island displacement and quantitative dependence of the rate of displacement on the island size yields both the mechanism and the magnitude of the force (*9*).

To study these two cases, it was necessary to maximize the current density j while minimizing Joule heating, which otherwise drives the rates of nanostructure evolution past the point of observability by STM. The Ag thin film is shadow mask–patterned in stripes, with a width of ~50 μm and thickness of ~350 nm (Fig. 1C). The stacks of adatom islands or vacancy islands range in height (or depth) from five to eight monatomic layers (Fig. 1D). Starting with this surface morphology, we applied direct current to the stripes. After thermal stabilization (about 30 to 40 min), we located the STM tip onto the middle area of the stripe and then measured the displacement of monatomic islands with the direct current still applied. Additional precautions relevant for these STM measurements are discussed in (*10*). For the step-bending measurements, samples were also prepared with precisely controlled C_{60} decoration of the step edges (*11*).

At a current density of 6.7×10^9 A/m^2 and a sample temperature of 318 K (*10*), the biased displacement can be observed by comparing sequential STM images, as in the still frames, from movie S1, shown in Fig. 2.

These results are quantified in Fig. 3, in which the COM of the islands is shown as a function of time for current applied in the positive and negative y directions. The initial position of the front edge of each island is shown by the horizontal line. The biased displacement is demonstrated by the strong anisotropy of the displacements in the parallel and the perpendicular directions (y and x), which is dramatically different from Brownian motion of islands without a biasing current (*12*). In the perpendicular (x) direction, there is no net displacement. In the parallel (y) direction, the measured displacement is up to 90 nm, limited by the time for the islands to totally decay (~1700 s). The island displacement is parallel to the direction of electron flow. During the measurements, the island area decreases linearly with time (Fig. 3B), which is similar to the linear decay behavior of isolated islands (*13*) and different from the nonlinear decay of islands bounded by three-dimensional stacks of concentric terraces (*14*, *15*). The island decay provides a natural method for evaluating the dependence of the drift velocity on island size, for comparison with theoretical prediction (*9*).

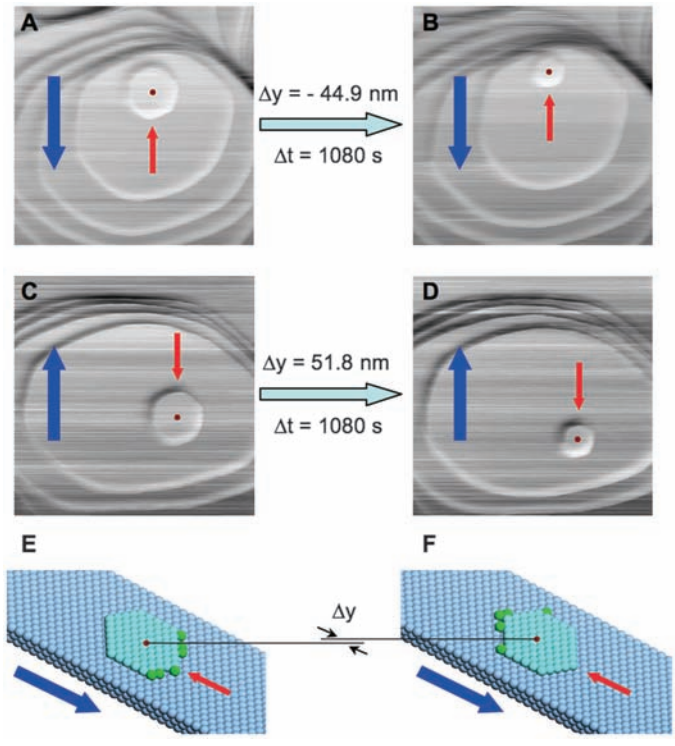

Fig. 2. Biased displacement of monolayer islands driven by electromigration force at $T = 318$ K. Shown for comparison are image pairs for monolayer islands that were measured in exactly the same area but with different current directions. In (**A**) and (**B**), in which the current direction is downward, the island displacement is upward, whereas the island displacement is downward in (**C**) and (**D**), in which the current direction is upward. The shrinking island size seen in both pairs of images is a thermal effect; the same shrinking occurs at this temperature without the electrical current present. The blue arrows indicate the direct current direction, and the orange arrows indicate the direction of electron flow. The image size is (500 × 500) nm^2. (**E**) and (**F**) schematically illustrate the island displacement that is due to the force on edge atoms, in which the blue atoms are the substrate, the lighter blue atoms are those in the bulk of the island, and the green atoms are diffusing edge atoms of the island. The small dark red dot indicates the COM of the monolayer island in (A) to (F).

From the displacement measurements, the drift velocity of the islands was calculated by averaging the slopes of two adjacent position-time points without smoothing. The range of island velocities is from 0.02 nm/s to 0.12 nm/s, which can be compared with the step velocity at copper (Cu) grain boundaries of ~5 nm/s at approximately four-times-larger current density (*16*). The correlation of the velocities with the island radii is presented in Fig. 3C and shows a strong velocity-radius dependence. The black solid line is a one-parameter fit of the experimental data to $v = C/R$, where C is a physical constant (Eq. 1) and R is the island radius, yielding $C = 1.93 \pm 0.09$ nm^2/s. An inverse radius dependence of the velocity has been predicted for island displacement biased by motion of atoms around the edges of the island (*9*) in contrast with the constant velocity predicted for a pure attachment/detachment mechanism. An edge-diffusion mechanism is also consistent with previous measurements (*17*) of island edge and step fluctuations on Ag(111), which have shown that the dominant mode of Ag mass transport is via edge diffusion in this temperature range. Lastly, the measured decay rate [$dA/dt = -B$, where B is a physical constant (*10*)] and COM velocity ($v = C/R$) for the circular islands was combined and integrated to yield the time-dependent positions of the front and back edges of the island, as shown by the solid curves in Fig. 3D. These results confirm the mechanism of island displacement as step-edge diffusion and thus the origin of the electromigration force as electron collisions.

The expression for the island drift velocity resulting from atomic diffusion around the edges is (*9*)

$$v = -\frac{aD_L F}{k_B T R} \quad (1)$$

where a is the lattice constant. Given the measured product of v and R above, and assuming an isotropic island edge, F can be calculated given the edge diffusion constant D_L. Previous measurements of step fluctuation dynamics (*18*) and calculations of the island-edge free energy (*19*) show that the value of D_L depends strongly on the orientation of the island edge (*10*). The edge diffusion constant for high-symmetry (straight) step edges is $D_{L,s} = 1.8 \times 10^4$ nm^2/s, whereas diffusion on low-symmetry (rough) step edges is much more difficult, with an average value of $D_{L,r} = 4.1 \times 10^2$ nm^2/s, with uncertainty (1 SD) of ~40% on the values. The actual island shape consists of straight edges joined by rounded corners. A lower limit for F can be obtained by assuming the largest diffusion constant, that of the straight edges, yielding $|F_{min}| = 0.012$ meV/nm ($|F_{min}/j_{bulk}| = 1.8 \times 10^{-4}$ eV cm/A, where j_{bulk} is the bulk current density). However, the diffusing atoms must traverse the rough regions of the island edge in series with the straight regions, suggesting that a higher value of F is needed to generate the measured island speed. Analysis of

the island shape (*10*) shows that ~27% of the island edge is rough. Calculating an effective diffusion constant as $1/D_{L,eff} = 0.73/D_{L,s} + 0.27/D_{L,r}$ gives $D_{L,eff} = 1.4 \times 10^3$ nm^2/s, and the corresponding F magnitude is 0.15 ± 0.06 meV/nm. Normalizing this to the bulk current density gives $|F/j_{bulk}| = 2.2 \times 10^{-3}$ eV cm/A.

This value is strikingly larger than the expected force on a step on Ag(111), which should be approximately one and a half to two times as large as that for a Ag adatom on Ag(111) (*20*), for which $|F/j_{bulk}| = 3.0 \times 10^{-5}$ eV cm/A. It is also larger than calculated values in other systems, such as for vacancy migration in Cu (*21*), for which $|F/j_{bulk}| = 6.6 \times 10^{-5}$ eV cm/A, or the scattering force in a single-atom-wide chain of silicon (Si) atoms, for which $|F/j_{bulk}| \cong 1 \times 10^{-4}$ eV cm/A (*22*). Instead, the magnitude of F/j_{bulk} is comparable with calculations for ions in carbon nanotubes (*4*) gated into strong conductance and is consistent with estimates that are based on experimental measurement of the electromigration-biased fluctuations of steps on Ag(111) (*23*). These values are shown in Table 1.

We modified the electronic environment of the step edge (*24*) by means of adsorption of C_{60}, which is known to withdraw electrons from Ag (*25*). C_{60} decorates step edges, and qualitative observation of the morphology of the decorated surface shows dramatic changes under the same current density (6.7×10^9 A/m^2) (*10*). The decorated steps change orientation, with the steps moving from the perpendicular to parallel to the current direction during observation. To quantify this effect, we identified pinned steps in which step curvature is reproducibly altered by the electromigration force (Fig. 4A). The arrow in each image indicates the current direction. The step bends against the current direction, and thus in the direction of the electron flow, so that the decorated step looks like a sail bowing under the wind. Similarly to the equilibrium (no current)–decorated island edges (*11*), the decorated steps here also fluctuate. To obtain the steady-state configuration (Fig. 4B), more than 10 images were averaged to quantify each configuration.

The changes in step shape are caused by displacement of Ag atoms under the electromigration force, which is equivalent to an imposed gradient in chemical potential (*26*)

$$F = -d\mu/dx \qquad (2)$$

where F is applied in the x direction and μ is the local chemical potential. Atomic motion under this chemical potential gradient will be opposed by the Gibbs-Thomson effect, which is the change in step chemical potential attributable to curvature. On (111) surfaces, the explicit relation between the step chemical potential and the curvature κ is

$$\mu = -\frac{\sqrt{3}}{2}\tilde{\beta}a^2\kappa \qquad (3)$$

where $\tilde{\beta}$ is the step stiffness. From our previous study on decorated island fluctuations, we have $\tilde{\beta} = 0.65$ eV/nm (*11*, *27*). Given the smooth step shape, we can determine the local curvature of the step configurations. The solid lines in Fig. 4B are polynomial fits to the experimental data, from which we can calculate the curvature along the step. The resulting force magnitude is $F = 1.30 \times 10^{-2}$ meV/nm ($|F/j_{bulk}| = 1.9 \times 10^{-4}$ eV cm/A), which is obtained by averaging the two config-

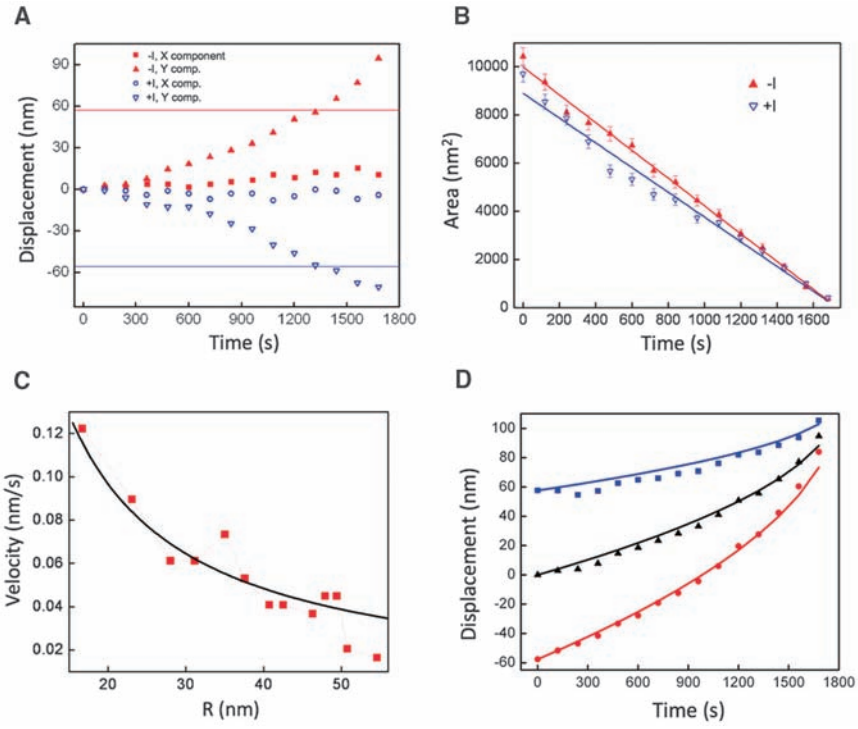

Fig. 3. (**A**) The displacement of island mass centers as a function of time. Here the *y* axis is parallel to the current direction, and the *x* axis is perpendicular to the current direction. The red and blue data (*–I* and *+I*) correspond to current in the *y*– and *y*+ directions, respectively. The horizontal lines indicate the initial position of the front edge of each island. (**B**) Island areas as a function of time. The solid lines are linear fits and yield the decay rate –5.76 ± 0.11 (nm^2/s) for the *–I* direction island and –5.13 ± 0.20 (nm^2/s) for the *+I* direction island. (**C**) Drift velocity as a function of the island radius. The solid black line is one parameter fit, $v = C/R$. The best fitting parameter is $C = 1.93 \pm 0.09$ (nm^2/s). (**D**) The position of the front edge (squares), COM (triangles), and back edge (circles) of the *–I* direction island. The curves are calculated by integrating the two relationships $dA/dt = -B$ and $v = C/R$ (Eq. 1) and using the measured values of $B = 5.8$ nm^2/s and $C = 1.9$ nm^2/s.

Table 1. Comparison of representative values of the electromigration force, shown using several commonly used presentations: F/j_{bulk}, $z^* = F/ej_{bulk}\rho_{bulk}$, and $\sigma_{eff} = Fe/mv_F j_{bulk}$, where e is the magnitude of the electron charge. The values shown for the clean island edge include the effects of edge roughness. The lower limits obtained by neglecting edge roughness are 1/12.5 times smaller.

System	$\lvert F/j_{bulk}\rvert$ (eV cm/A)	$\lvert z^*\rvert$	σ_{eff} (nm^2)	Reference
Vacancy in bulk Cu, calculated	6.6×10^{-5}	39	1.2×10^{-2}	(*20*)
Ion in gated carbon nanotube, calculated	~1.3×10^{-3}			(*4*)
Atomic Si wire, calculated	~1.1×10^{-4}			(*21*)
Ag atom on Ag(111), calculated	3.0×10^{-5}	17	6.1×10^{-3}	(*19*)
Step edge on Al, calculated		43		(*27*)
Step edge on Ag(111), measured		85 to 255 (lower limit)	0.03 to 0.09	(*22*)
Island edge site on Ag(111), measured	$(2.2 \pm 0.9) \times 10^{-3}$	1260 ± 500	4.5×10^{-1}	This work
C_{60}-decorated step edge on Ag(111), measured	1.9×10^{-4}	111	3.9×10^{-2}	This work

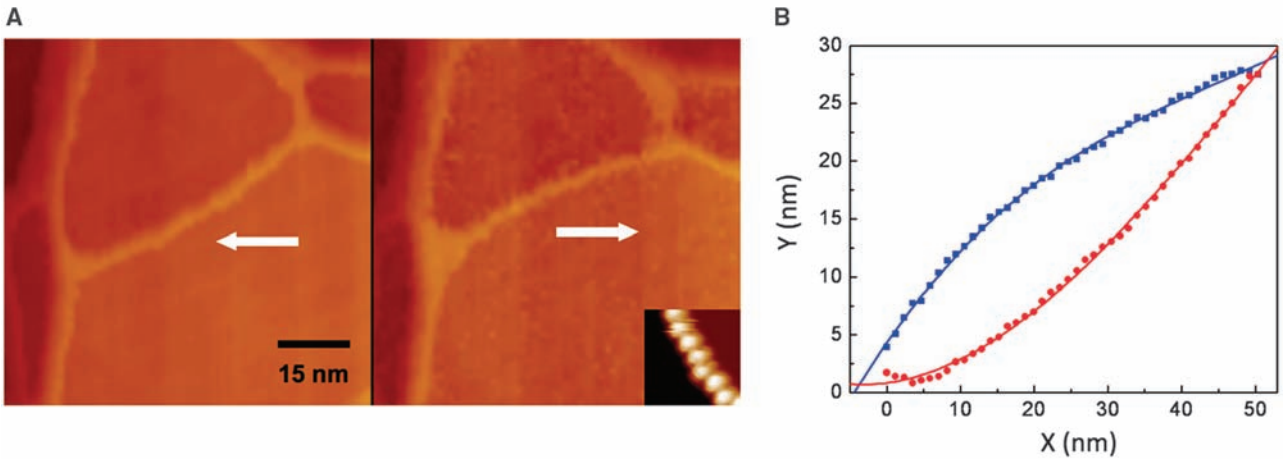

Fig. 4. (**A**) STM images of the steady-state configuration of a C_{60}-decorated step under applied current in two opposing directions. (Inset) Molecular structure of the chain of C_{60} molecules. (**B**) Quantified configuration of the decorated steps in (A). Each configuration is obtained by averaging more than 10 images. The red circles and the blue squares are for the left and right configurations shown in (A), respectively.

urations. So, the force acting on the decorated steps is comparable with the lower limit and smaller, by slightly more than 1 SD, than the best value determined for the electromigration wind force on the bare island edges. However, it is still substantially larger than calculated values for electromigration in metals, and in particular about a factor of 4 larger than the expected value for a clean step on Ag(111).

Unlike macroscopic measurements of electromigration effects, the forces measured here are identified with a specific atomic structure—in this case, that of kink sites (for example, positions where thermal excitation has displaced an atom from the low-energy configuration) at a step. This provides an opportunity to understand this force from first principles. In the classical description, the surprisingly large magnitude in this case can arise from at least three effects: current crowding, changes in scattering cross section, and changes in local electron density. Current crowding, the variation of local current density near constrictions in flow path, can cause local increases of up to about a factor of 2 in extreme geometries (*21*); however, the constriction due to current flow around the island edge is likely to be more modest. The steps of the edge of the island themselves can act as a reflecting barrier, increasing the cross section for scattering as compared with a free atom on the surface by about a factor of at least 1.5 for Al(001) (*28*). Lastly, atomic relaxation at step edges causes redistribution of local charge density (*29*, *30*), with especially strong enhancement—up to a factor of 10 on Cu(532)—near kink sites (*24*). Surface states near steps could influence the magnitude of the electromigration force by increasing or decreasing the electron density near the Fermi level. However, a reported unoccupied state on Ag(111) occurs well above the Fermi level (*31*) and thus should not affect the behavior of the electrons involved in transport, which are near the Fermi level.

The combination of these three effects therefore may account for up to a factor of 20 increase in the force on kink-site atoms at the island edge as compared with that of a free Ag atom. Using the value for Ag/Ag(111) in Table 1, this yields a force magnitude up to ~10^{-3} eV cm/A, which is slightly more than 1 SD below the measured value of $(2.2 \pm 0.9) \times 10^{-3}$ eV cm/A for the bare island edges. The measured force decreases with the addition of C_{60}, possibly through a reduction in local valence electron density because of charge transfer to the C_{60} or as a result of changes in the local kink geometry. Because the kink scattering site is much smaller than the mean free path of the transport electrons, the effects described above should be understood more directly in the context of Landauer ballistic conduction (*32*), coupled with nonequilibrium transport calculations (*33*). In Landauer ballistic conduction, the local current density rather than the bulk electric field defines the scattering environment, and there is a local potential drop at each scatterer. The corresponding dipole was first observed directly by using scanning tunneling potentiometric (STP) imaging of 5- to 10-nm-scale defects on a thin bismuth (Bi) film under current bias (*34*), and a more recent observation of a Ag film on Si has associated potential drops with specific step resistivities (*35*). First-principles calculations of the electronic structure at defect sites within a nonequilibrium transport formalism should yield the transmission coefficients for the defect sites directly, allowing a full understanding of the variability of the electromigration force with atomic scale structure.

The mechanisms proposed here to explain the large electromigration force are generally applicable to defects at surfaces and interfaces. Thus, we predict that the large forces revealed in this atomically specific measurement of the effects of electron scattering at island-edge kink sites will be a common nanoelectronic effect that is due to ubiquitous interfacial defect structures at the nanoscale (*3*, *16*, *36*–*38*). As a result, interesting structural transformations because of kinetic instabilities, previously thought to require onerously large current densities (*39*), may be more generally accessible. The enhanced electron scattering will also couple into nanoelectronic transport characteristics, with implications for reliability, noise, switching, and possibly stochastic resonance. These and more exotic possibilities, such as harnessing the electromigration force for work (*40*), will be predictable as continuing experimental and theoretical work leads to a full understanding of the relation between atomic structure and scattering strength.

References and Notes

1. P. S. Ho, T. Kwok, *Rep. Prog. Phys.* **52**, 301 (1989).
2. H. Yasunaga, A. Natori, *Surf. Sci. Rep.* **15**, 205 (1992).
3. H. Park, A. K. L. Lim, A. P. Alivisatos, J. Park, P. L. McEuen, *Appl. Phys. Lett.* **75**, 301 (1999).
4. S. Heinze, N.-P. Wang, J. Tersoff, *Phys. Rev. Lett.* **95**, 186802 (2005).
5. O. Pierre-Louis, *Phys. Rev. E Stat. Nonlin. Soft Matter Phys.* **76**, 062601 (2007).
6. E. D. Williams *et al.*, *N. J. Phys.* **9**, 387 (2007).
7. T. Taychatanapat, K. I. Bolotin, F. Kuemmeth, D. C. Ralph, *Nano Lett.* **7**, 652 (2007).
8. T. Kizuka, H. Aoki, *Appl. Phys. Express* **2**, 075003 (2009).
9. O. Pierre-Louis, T. L. Einstein, *Phys. Rev. B* **62**, 13697 (2000).
10. Materials and methods are available as supporting material on *Science* Online.
11. C. Tao, T. J. Stasevich, W. G. Cullen, T. L. Einstein, E. D. Williams, *Nano Lett.* **7**, 1495 (2007).
12. K. Morgenstern, E. Laegsgaard, F. Besenbacher, *Phys. Rev. Lett.* **86**, 5739 (2001).
13. K. Morgenstern *et al.*, *Phys. Rev. B* **63**, 045412 (2001).
14. K. Thurmer *et al.*, *Phys. Rev. Lett.* **87**, 186102 (2001).
15. A. Ichimiya *et al.*, *Phys. Rev. Lett.* **84**, 3662 (2000).
16. K. C. Chen, W. W. Wu, C. N. Liao, L. J. Chen, K. N. Tu, *Science* **321**, 1066 (2008).
17. M. Giesen, *Prog. Surf. Sci.* **68**, 1 (2001).
18. C. Tao, T. J. Stasevich, T. L. Einstein, E. D. Williams, *Phys. Rev. B* **73**, 125436 (2006).
19. T. J. Stasevich *et al.*, *Phys. Rev. B* **71**, 245414 (2005).
20. M. F. G. Hedouin, P. J. Rous, *Phys. Rev. B* **62**, 8473 (2000).
21. J. Hoekstra, A. P. Sutton, T. N. Todorov, A. Horsfield, *Phys. Rev. B* **62**, 8568 (2000).
22. Z. Q. Yang, M. Di Ventra, *Phys. Rev. B* **67**, 161311 (2003).
23. O. Bondarchuk *et al.*, *Phys. Rev. Lett.* **99**, 206801 (2007).
24. F. Mehmood, A. Kara, T. S. Rahman, *Surf. Sci.* **600**, 4501 (2006).
25. L. Wang, H. Cheng, *Phys. Rev. B* **69**, 165417 (2004).
26. K. Thurmer, D. J. Liu, E. D. Williams, J. D. Weeks, *Phys. Rev. Lett.* **83**, 5531 (1999).

27. T. J. Stasevich, C. G. Tao, W. G. Cullen, E. D. Williams, T. L. Einstein, *Phys. Rev. Lett.* **102**, 085501 (2009).
28. P. J. Rous, *Phys. Rev. B* **59**, 7719 (1999).
29. Y. N. Mo, W. G. Zhu, E. Kaxiras, Z. Y. Zhang, *Phys. Rev. Lett.* **101**, 216101 (2008).
30. J. Y. Park *et al.*, *Phys. Rev. Lett.* **95**, 136802 (2005).
31. A. Sperl *et al.*, *Phys. Rev. B* **77**, 085422 (2008).
32. R. S. Sorbello, *Solid State Phys.* **51**, 159 (1997).
33. J. Taylor, H. Guo, J. Wang, *Phys. Rev. B* **63**, 245407 (2001).
34. B. G. Briner, R. M. Feenstra, T. P. Chin, J. M. Woodall, *Phys. Rev. B* **54**, R5283 (1996).
35. J. Homoth *et al.*, *Nano Lett.* **9**, 1588 (2009).
36. Y. Zhang, W. van Drongelen, B. He, T. Block, C. Tegenkamp, *Appl. Phys. Lett.* **89**, 223903 (2006).
37. C. Jin, K. Suenaga, S. Iijima, *Nano Lett.* **8**, 1127 (2008).
38. T. Sun *et al.*, *Phys. Rev. B* **79**, 041402 (2009).
39. M. Rusanen, P. Kuhn, J. Krug, *Phys. Rev. B* **74**, 245423 (2006).
40. D. Dundas, E. J. McEniry, T. N. Todorov, *Nat. Nanotechnol.* **4**, 99 (2009).
41. This work has been supported by the University of Maryland NSF Materials Research Science and Engineering Center under grant DMR 05-20471, including use of the Shared Experimental Facilities. Infrastructure support is also provided by the University of Maryland NanoCenter and the Center for Nanophysics and Advanced Materials.

Supporting Online Material
www.sciencemag.org/cgi/content/full/328/5979/736/DC1
Materials and Methods
Figs. S1 to S4
References
Movie S1

4 January 2010; accepted 7 April 2010
10.1126/science.1186648

Viscosity of $MgSiO_3$ Liquid at Earth's Mantle Conditions: Implications for an Early Magma Ocean

Bijaya B. Karki[1]* and Lars P. Stixrude[2]

Understanding the chemical and thermal evolution of Earth requires knowledge of transport properties of silicate melts at high pressure and high temperature. Here, first-principles molecular dynamics simulations show that the viscosity of $MgSiO_3$ liquid varies by two orders of magnitude over the mantle pressure regime. Addition of water systematically lowers the viscosity, consistent with enhanced structural depolymerization. The combined effects of pressure and temperature along model geotherms lead to a 10-fold increase in viscosity with depth from the surface to the base of the mantle. Based on these calculations, efficient heat flux from a deep magma ocean may have exceeded the incoming solar flux early in Earth's history.

Silicate liquids likely played a crucial role in terrestrial mass and heat transport in Earth's history. Molten silicates would have controlled the dynamics of the predicted magma ocean [a largely or completely molten mantle that is expected during Earth's earliest stages (*1*)] and continue to influence the transport of modern magmas at the present. If such a magma ocean existed, the rates of initial thermal evolution (via convection) and chemical evolution (via crystal settling and melt percolation) of Earth's interior would be primarily controlled by the melt viscosity (*2*). The ability of melts to carry xenoliths from great depths in the mantle (*3*) also depends on the melt viscosity, in addition to melt composition. Moreover, melts are considered to be responsible for the ultralow velocity zone (ULVZ) in the deep mantle detected by seismology (*4*, *5*).

Despite their importance, transport properties, including the viscosity of molten silicates, are unknown over almost the entire mantle pressure regime, which reaches 136 GPa at the core-mantle boundary. Because of experimental difficulties, the viscosity of $MgSiO_3$ liquid, the dominant composition of Earth's mantle, has only been measured at ambient pressures (*6*). In fact, viscosity measurements of any silicate melts have been limited to relatively low pressures (<13 GPa) (*7*–*12*). In many silicate liquids, the viscosity depends non-monotonically on pressure over the range that has been measured, making extrapolations highly uncertain. Theoretical computations serve as a complementary approach. Previous calculations were primarily based on atomistic models (*13*–*15*), which permit much faster computation but have the disadvantage of being based on empirical force fields, the forms of which are uncertain. On the other hand, the first-principles approach is more robust because it makes no assumptions about the nature of bonding or the shape of the charge density and is thus in principle equally applicable to the study of a wide variety of materials problems, including liquids. We previously calculated the structure and thermodynamic properties of $MgSiO_3$ and $MgSiO_3$-H_2O liquids from first principles (*16*, *17*), finding good agreement with extant experimental data over the entire mantle pressure-temperature regime. Unlike these equilibrium properties, the transport properties such as viscosity require much longer simulation (*18*).

Here, we determine the viscosity of two key liquids over the entire mantle pressure regime from density functional theory (*18*). $MgSiO_3$ serves as an analog composition for a magma ocean, whereas $MgSiO_3$-H_2O liquid allows us to explore the role of melt composition, focusing on H_2O as the component that is known to have the largest influence on the viscosity at low pressure (*19*). The shear viscosity (η) was calculated by using the Green-Kubo relation

$$\eta = \frac{V}{3k_B T}\int_0 \left\langle \sum_{i<j} \sigma_{ij}(t+t_0).\sigma_{ij}(t_0) \right\rangle dt \quad (1)$$

where σ_{ij} (i and $j = x, y, z$) is the stress tensor, which is computed directly at every time step of the simulation, V is volume, k_B is the Boltzmann constant, T is temperature, t is time, and t_0 represents the time origin. The shear-stress autocorrelation function (the integrand of Eq. 1) decays to zero more slowly at lower temperature and higher pressure, requiring longer simulation

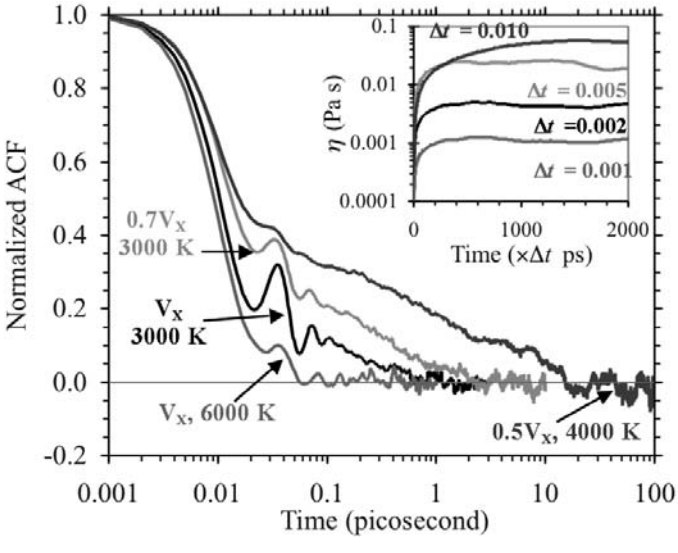

Fig. 1. Time convergences of the calculated stress autocorrelation function (ACF) and viscosity (**inset**) of $MgSiO_3$ melt (without water) at different conditions. The run durations are 18 ps (V_X, 6000 K, 7.5 GPa), 60 ps (V_X, 3000 K, 1.8 GPa), 72 ps ($0.7V_X$, 3000 K, 25 GPa), and 172 ps ($0.5V_X$, 4000 K, 135 GPa), where V_X is the reference volume (38.9 cm^3mol^{-1}).

[1]Department of Computer Science, Department of Geology and Geophysics, Louisiana State University, Baton Rouge, LA 70803, USA. [2]Department of Earth Sciences, University College London, London WC1E 6BT, UK.

*To whom correspondence should be addressed. E-mail: karki@csc.lsu.edu